

# Spatial pattern and seasonal dynamics of the photosynthesis activity across Australian rainfed croplands

Jianxiu Shen<sup>a,b,\*</sup>, Alfredo Huete<sup>b</sup>, Xuanlong Ma<sup>b,c</sup>, Ngoc Nguyen Tran<sup>b</sup>, Joanna Joiner<sup>d</sup>, Jason Beringer<sup>e</sup>, Derek Eamus<sup>b</sup>, Qiang Yu<sup>b,f,g</sup>

<sup>a</sup> Big Data in Agriculture, Murdoch University, WA 6150, Australia

<sup>b</sup> School of Life Sciences, University of Technology Sydney, NSW 2007, Australia

<sup>c</sup> College of Earth and Environmental Sciences, Lanzhou University, Lanzhou 730000, China

<sup>d</sup> Laboratory for Atmospheric Chemistry and Dynamics, NASA Goddard Space Flight Center, Greenbelt, MD 20771, USA

<sup>e</sup> School of Earth and Environment, The University of Western Australia, Crawley, WA 6009, Australia

<sup>f</sup> State Key Laboratory of Soil Erosion and Dryland Farming on the Loess Plateau, Northwest A&F University, Yangling 712100, China

<sup>g</sup> College of Resources and Environment, University of Chinese Academy of Science, Beijing 100049, China

## ARTICLE INFO

### Keywords:

Agricultural remote sensing  
Solar-induced chlorophyll fluorescence  
Enhanced vegetation index  
Light-use efficiency  
Australian rainfed croplands

## ABSTRACT

Early detection of crop water and heat stress for effective crop management requires continuous and accurate monitoring of cropland photosynthesis activity. Satellite measurements can complement the restrictive coverage afforded by *in-situ* measurements and have the potential to facilitate the monitoring of cropland photosynthesis over a large spatial scale in a cost-effective manner. Traditionally, space-based monitoring of cropland photosynthetic activity, especially Light-use efficiency (LUE), has relied on empirical relationships between satellite spectral reflectance and ground climate and vegetation conditions. Space-borne retrievals of sun-induced chlorophyll fluorescence (SIF), an independent measurement, has shown to provide a more direct estimation of photosynthetic activity than traditional methods, and may further allow the inference of LUE.

This study has empirically explored the possibility of remotely monitoring large-scale LUE by calculating the ratio of photosynthetically active radiation (PAR) normalized SIF to the Enhanced Vegetation Index (EVI). We applied this calculation to demonstrate the spatial patterns and seasonal dynamics of LUE and its related measurements in response to land surface temperature (LST) across Australian rainfed croplands from 2007 to 2016. LST was used to provide an integrated measure of vegetation water and heat stress at the canopy level.

Our results showed that LUE tends to be higher in the geographical middle zones than in either the warmer northern or the cooler southern regions. Temporally, we found that there was a seasonal asymmetry of LUE and its related measurements in response to LST change throughout the winter crop-growing season. Statistical tests revealed that the optimum LST range for satellite-based LUE was 16.6–17.6 °C during August. The more LST exceeded this optimum, the more sensitive LUE was found to be. Pixels in August with optimum LST across the ten-year sampling period (Augusts of 2007–2016) were distributed in the southern-middle to middle zones of the Australian rainfed croplands.

Our results provide new opportunities for large-scale cropland heat and drought stress detection under a future warmer and drier climate and can also support remote analyses of crop photosynthetic activity over large spatial scales.

## 1. Introduction

Accurate estimation of large-scale vegetation gross primary production (GPP) has both theoretical and practical significance. Light-use efficiency (LUE) describes the photosynthesis rate, the efficiency of the conversion of photosynthetically active radiation (PAR) absorbed by

vegetation (APAR) to GPP (Gitelson et al., 2015). Continuous and direct monitoring of cropland LUE can help forecast crop productivity and can also assist in providing a better understanding of the responses of crop growth to environmental change. The physiological concept of LUE model was originally defined by Monteith (1972, 1977); Since then, it has been widely used in most current GPP estimation models.

\* Corresponding author at: Big Data in Agriculture, Murdoch University, WA 6150, Australia.

E-mail address: [Jenny.Shen@murdoch.edu.au](mailto:Jenny.Shen@murdoch.edu.au) (J. Shen).

<https://doi.org/10.1016/j.ecolind.2019.105669>

Received 14 November 2018; Received in revised form 13 August 2019; Accepted 21 August 2019

1470-160X/© 2019 Elsevier Ltd. All rights reserved.

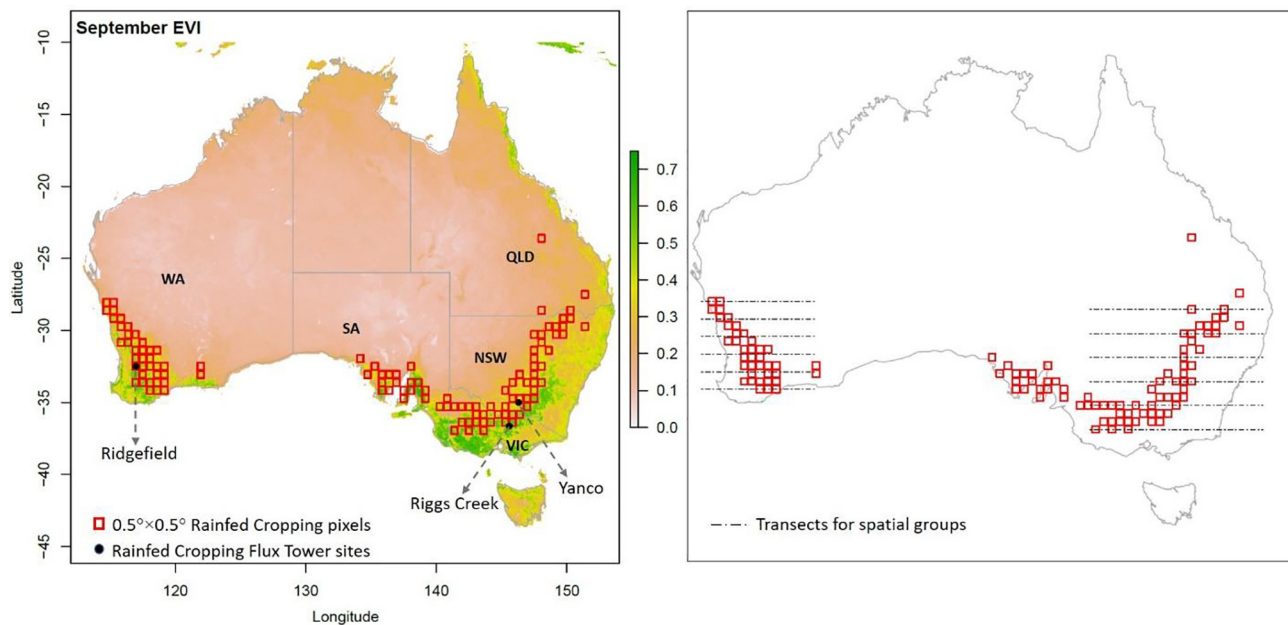


**Fig. 1.** Australian rainfed croplands in different levels of spatial resolution (left) and the spatial groups of testing pixels (right). The white to green color range in the left panel is the ten-year (2007–2016) mean MODIS EVI map during September. Western Australia (WA), South Australia (SA), Victoria (VIC), New South Wales (NSW), Queensland (QLD), and Northern Territory (NT) are the seven states and territories in Australia. The five groups of pixels between the transects dividing each of the two major Australian cropland belts in the right panel are designated as the following zones: (1) Southern, (2) Southern-Middle, (3) Middle, (4) Northern-Middle, and (5) Northern.

In most current studies, LUE was calculated by down-regulating the maximum LUE with scalars of water and heat stress (Sims et al., 2008; Dong et al., 2015), or parameterized as a function of meteorological parameters for a given biome (Xiao et al., 2008; Wang et al., 2010; Running et al., 2004). In these cases, LUE models rely heavily on the parameterization of many physiological limiting factors such as temperature and soil moisture (Hilker et al., 2008). The more factors are present in a model, the more measurements and calibrations are required. As a result, the model may become more complex and consequently subject to more systematic errors (Sjöström et al., 2011; Yuan et al., 2010).

Practically, LUE is site and biome dependent and can be affected by a number of processes (Gitelson and Gamon, 2015), ranging from chlorophyll pigment composition, enzyme kinetics, and stomatal conductance (Gamon and Qiu, 1999; Yan et al., 2017), to changes in vapor pressure deficit, and drought stress (Dong et al., 2015). Consequently, LUE varies dynamically over multiple temporal and spatial scales with changing environmental conditions. This makes it difficult to continuously and rapidly parameterize all changing environmental variables throughout the life span of vegetation.

To overcome these challenges, efforts have been made to estimate vegetation photosynthesis activity entirely from remotely sensed variables without any ground-based inputs. In this case, the MODerate-resolution Imaging Spectroradiometer (MODIS)-GPP model (Zhao et al., 2005; Running et al., 1999) has been well established as mean of estimating global GPP from space. However, the LUE values of the MODIS-GPP model are obtained from look-up tables for individual biomes within each pixel. These look-up tables were obtained by parameterizing the factors of environmental stresses for a given biome. Whereas, there are also other efforts to avoid introducing the parameter of LUE in GPP estimation, including the enhanced vegetation index (EVI)-based Temperature and Greenness (TG) model (Sims et al., 2008) and the Vegetation Photosynthesis Model (VPM) (Yan et al., 2009; Xiao et al., 2005, 2004). These models do not include LUE as a parameter but rely on two key factors: land surface temperature (LST) and EVI, while VPM model also uses the land surface water index (LSW) as additional input. Admittedly, the measurement of LST taken via infrared

thermography can adequately estimate the integrated stress from the meteorological variables without explicitly considering each of them individually (Idso et al., 1977; Sims et al., 2008). Therefore, the LST for photosynthetic activity in the LST-based GPP estimation models were established as being within the 20–30 °C range based on the research by Berry and Bjorkman (1980). However, the extent to which the optimum LST range changes seasonally with different phenological stages remains unclear.

A newly emerging remote sensing retrieval technique, solar-induced fluorescence (SIF), offers great potential for advancing our capacity to directly measure the photosynthetic status of vegetation (Joiner et al., 2014; Guan et al., 2016; Jeong et al., 2017). The fluorescence signal observed by the spaceborne remote sensing system is the active emission of light quanta from the vegetation canopy. This signal is directly linked to photosynthesis activity. Chlorophyll fluorescence emission displays two peaks near 685 and 740 nm in the red and far-red wavelengths respectively (Joiner et al., 2011; Campbell et al., 2008). Liu and Cheng (2010) highlighted that LUE can be detected more directly through the separation of the SIF signal from the hyperspectral data. However, Liu et al. (2013) found that the LUE-SIF relationship is clearly affected by canopy and environmental conditions. In light of this, satellite SIF observes the integral at a specific excitation wavelength (for a specific remote sensing instrument) contributed by all active chlorophyll photosynthesis at the canopy level. Therefore, satellite SIF signals contain information about not only leaf-level photosynthetic activity but also canopy structure, canopy chlorophyll content, and canopy greenness (Yang et al., 2017). As EVI was conducted as an effective index for measuring the level of vegetation greenness from space (Huete, 2012; Yang et al., 2013; Xiao et al., 2005), we introduced EVI in this study to remove the effects of vegetation canopy conditions on SIF-based LUE estimation.

The aims of this study were as follows: 1) to approximate LUE remotely across broadacre rainfed croplands using satellite SIF and EVI; 2) to characterize the spatial pattern and inter-seasonal dynamics in the estimated LUE and its related measurements of winter wheat cropland in Australia; and 3) to examine the intra-seasonal variation of LUE in response to LST during the crop growing season.

**Table 1**  
Details of the three Australian eddy flux sites.

Name	Location (Lat/Long)	Monitoring Period	Annual Rainfall	Temperature Range	Land Cover	State
Riggs Creek	−36.6499, 145.5760	Jan 2011–Oct 2015	650 mm	12–26 °C	Dryland Agriculture	Victoria
Ridgefield	−32.5061, 116.9668	Mar 2016–Nov 2016	446 mm	5.5–31.9 °C	Dryland Agriculture	Western Australia
Yanco	−34.9893, 146.2907	Oct 2012–Dec 2016	465 mm	12–37 °C	Dryland Agriculture	New South Wales

## 2. Material and methods

### 2.1. Study area

The Australian rainfed croplands extend in the form of a crescent along the western, southern, south-eastern, and eastern parts of mainland Australia (Fig. 1). The croplands comprise two major land belts: the western belt (WA) and the eastern belt (NSW and VIC). The climate conditions are temperate to subtropical, with a mean annual temperature of 14 °C–26 °C and annual precipitation of 250 mm–1500 mm (Dan et al., 2007). Planting winter wheat is the major farming activity across the Australian rainfed cropland (Hochman et al., 2017). The average growing season of winter wheat in Australia extends from late May to November (Bowden et al., 2008). September is the average crop heading time. Thus, a distinct seasonality of vegetation growth can be observed from space. Fig. 1(-left) shows the ten-year average EVI for September (2007–2016) across Australia with 0.05° spatial resolution. We observed that the September EVI values in the rainfed croplands were greater than those in the rest of the Australian ecosystems. In addition, the average cropland EVI in September was greater than the cropland EVI in other months. The peak EVI month divides the growing season observed from space into the vegetative growth stage and the reproductive growth stage (Broich et al., 2015; Shen et al., 2018).

To distinguish rainfed cropland from irrigated cropland, we obtained the Dynamic Land Cover Dataset (DLCD version 2) for Australia from Geoscience Australia (<http://www.ga.gov.au/>). This dataset is produced based on 16-day MODIS EVI composite at a 250-meter resolution during 2002–2010 (Lyburner et al., 2010). It has a high degree of consistency (93%) with extensive independent field-based investigations. To select effective rainfed cropland pixels at 0.5° × 0.5° resolution, we aggregated the 250-m resolution land use classification map using the majority resampling method. The purpose of resampling the fine resolution map to a coarse one (see red boxes in Fig. 1(-left)) was to facilitate comparison with the satellite-SIF dataset. The majority land cover type (> 70%) within each larger (0.5° × 0.5°) pixel was designated as the land cover type for that pixel. Based on the aggregated map, 111 pixels (red boxes) were identified and classified as rainfed cropping across the study area.

### 2.2. Data collection and pre-processing

#### 2.2.1. Satellite SIF retrievals

The global satellite-SIF retrievals were obtained from the Global Ozone Monitoring Experiment-2 (GOME-2) sensors on board the platform of Meteorological Operational Satellite-A (MetOp-A) during 2007–2016 (version 26) (Joiner et al., 2013). The GOME-2 SIF product was processed as a 0.5° × 0.5° spatial resolution monthly dataset with estimated errors of 0.1–0.4 mW m<sup>-2</sup> nm<sup>-1</sup> sr<sup>-1</sup> (Joiner et al., 2013). GOME-2 sensors currently provide the longest continuous SIF retrieval record, active since 2007. The overpass time of the MetOp-A platform is at around 9:30 am local time, which is close to the window of peak daily photosynthesis across Australian croplands (Guan et al., 2016). The cosine of the solar zenith angle was used as a proxy for the seasonal cycle of PAR (Joiner et al., 2014), and the level 3 global gridded monthly data (0.5° × 0.5°) with PAR normalization process (Joiner et al., 2013) were used.

#### 2.2.2. MODIS EVI and LST datasets

The monthly MODIS EVI (MOD13C2, collection 6) (Huete et al., 2002) and LST (MOD11C3) at 0.05° × 0.05° spatial resolution during 2007–2016 were downloaded from the Land Process Distributed Active Archive Center (LP DAAC) data pool, then processed by filtering out cloud covered observations. Both the MOD13C2 and MOD11C3 products were produced using the Terra observations, which has an overpass time of 10:30 am local time.

#### 2.2.3. Remote sensing-based GPP retrievals

The global vegetation GPP (non-forest) dataset for Australia was collected from Australian National Computational Infrastructure data collection (<http://nci.org.au/>) and provided by the Australian Water and Landscape Dynamics group at Australian National University (OzWALD, <http://www.wenfo.org/wald/>). This dataset, derived from MODIS remote sensing, has only two fitting parameters: radiation and canopy conductance limitations on GPP (Yebera et al., 2015). These GPP estimates have shown stronger or similar correlations to local GPP estimates from flux towers than current alternative GPP products. Details can be found in Yebera et al. (2015). We obtained the monthly cumulative GPP (in g C/m<sup>2</sup>/s) (2007–16) at a spatial resolution of 0.05° (accessible via <http://www.wenfo.org/wald/data-software/>).

#### 2.2.4. GPP observations from eddy-covariance flux tower sites

There are currently three eddy-covariance (EC) flux tower sites located in the Australian rainfed croplands, as shown in Fig. 1(-left) and Table 1. We collected carbon flux data from the OzFlux network (<http://www.ozflux.org.au/>) (Beringer et al., 2017).

The original carbon fluxes and other meteorological measurements were processed by means of the Dynamic IN-tegrated Gap-filling and partitioning for OzFlux (DINGO v13) program to align with half-hourly time series GPP data (Beringer et al., 2017). Monthly flux tower-measured GPP data were aggregated based on the half-hourly GPP data during the daytime and during the morning window of 09:00–11:00 am, separately. Here, daytime was defined as those half-hours that display active carbon uptake during a given day. Moreover, the reason for selecting a morning window from 09:00 to 11:00 am is to preserve the consistency of observation times from different sources of satellite data while ensuring that the instantaneous flux GPP data during that window can estimate daily GPP (Smith et al., 2018).

### 2.3. Experiment design

#### 2.3.1. Obtaining LUE from SIF and EVI

Current work (Guan et al., 2016; Guanter et al., 2014; Joiner et al., 2014) defines SIF and GPP as follows:

$$SIF(\lambda) = PAR \times fPAR \times LUE_F(\lambda) \times f_{esc}(\lambda) \quad (1)$$

$$GPP = PAR \times fPAR \times LUE_p \quad (2)$$

where  $\lambda$  is the excitation wavelength (~740 nm in the GOME-2 retrievals). PAR is the downwelling flux of photosynthetic-active radiation (400–700 nm) at the top of the canopy, while the term  $fPAR$  refers to the fraction of absorbed PAR.  $LUE_F$  is the light-use efficiency for SIF, which is the efficiency of fluorescence photons re-emitted from APAR.  $f_{esc}(\lambda)$  is the fraction of fluorescence photons escaping from the canopy surface.  $LUE_p$  is light-use efficiency for photosynthesis.

Due to the empirical significant linear relationship between GPP

and SIF was observed in many large-scale studies, especially in the late morning when many space-borne observations are made (Lu et al., 2018; Miao et al., 2018; Smith et al., 2018; Zhang et al., 2016, 2018).  $LUE_p$  is approximately proportional to the overall  $LUE_p$  of photosynthesis.

$$LUE_p = LUE_f(\lambda) \times f_{esc}(\lambda) \times a \quad \left( a = \frac{GPP}{SIF} \right) \quad (3)$$

In current reflectance-based GPP estimation models, the EVI is an effective measurement for canopy chlorophyll content. The fPAR within the photosynthetically-active period is estimated as a linear function of EVI with a coefficient of 1.0 (Lobell et al., 2002; Xiao et al., 2004, 2005; Yan et al., 2009; Garbulsky et al., 2008). Thus:

$$fPAR(EVI) = EVI \quad (4)$$

Because the reflectance signature of green leaves shows minimal absorbance in the near-infrared wavelengths (Gitelson and Merzlyak, 1996), and crops in growing season have a relatively simple plant structure and high leaf area index (Guan et al., 2016; Guanter et al., 2014), we assume that  $f_{esc}(\lambda) \approx 1$ . Therefore, we may expect the  $LUE_p$  to be estimated as:

$$LUE_p = \frac{SIF(\lambda)_{PAR}}{EVI} \times a \quad (5)$$

where  $SIF(\lambda)_{PAR}$  is the ratio of satellite SIF to PAR, while  $a$  is the constant ratio of GPP to SIF.

### 2.3.2. Spatial grouping based on geographical latitude

Rainfall, air temperature and solar radiation are direct defining and limiting factors of rainfed crop growth (Yu et al., 2001). LST measures the crop canopy temperature and represents an integral of crop stress from these meteorological variables (Shen et al., 2018). To test how LUE and its related measurements respond to LST change, we must take into account the spatial and seasonal variations in LST that arise not only from predictable seasonal changes in sunlight incident angle but also from variations in water and heat distribution across the land surface. As a result, we equally divided the range of latitudes encompassing the selected rainfed cropland pixels into five LST zones for each of the two major Australian cropland belts (Fig. 1(-right)). The eastern belt includes croplands in NSW and VIC, while the western belt includes WA croplands only. The five LST regions were then designated as follows: (1) Southern, (2) Southern-Middle, (3) Middle, (4) Northern-Middle, and (5) Northern, corresponding to regions from lower to higher mean annual temperature.

### 2.3.3. Intra-seasonal grouping based on LST percentage quantiles

As shown in Fig. 1, there were 111  $0.5^\circ \times 0.5^\circ$  pixels across the Australian rainfed croplands covering a range of LST values in a given month. At each pixel, ten LST values were recorded in the given month from 2007 to 2016. Consequently, there were a range of LST levels during each month ( $111 \times 10$ ), which reflect the spatial and intra-seasonal variations in water and heat conditions that can affect LUE. To examine these effect of LST variations on LUE, we divided the 1110 spatial-temporal LSTs in each month into 10 groups by percentage quantiles for the corresponding month.

### 2.3.4. Data incorporation

Data incorporation in this study includes four stages as follows:

- (1) to justify the experimental design and the utilization of datasets in different resolution, we aggregated the original MODIS EVI to  $0.05^\circ$ ,  $0.1^\circ$  and  $0.5^\circ$  resolutions and related them to EC site observations (GPP). If no great change in the regression determination coefficient ( $R^2$ ) was observed, and p-values remain significant ( $p < 0.01$ ) upon switching the MODIS EVI from a fine to a coarser resolution, the footprint of a flux tower may reach the coarser

resolution; otherwise, it remains limited to the finer resolution.

- (2) to calculate the LUE across Australian rainfed croplands based on Eq. (5), we have utilized the GOME-2 SIF products and the MODIS EVI products as the main inputs. The analyses were based on  $0.5^\circ$  spatial resolution at the monthly step. In determining the value of  $a$  in Eq. (5), we have incorporated the OzWALD-GPP datasets to ensure the resolution consistency. As such, the unit of  $a$  is calculated as the ratio of the units in OzWALD-GPP data to GOME-2 SIF data.
- (3) based on the derived remote sensing-based LUE, we analyzed the spatial pattern and the inter-seasonal variation of LUE and its related measurements. The spatial grouping method can be found in Section 2.3.2.
- (4) to identify the optimum LST range for LUE during each month of the growing season, we analyzed the intra-seasonal dynamics of LUE based on LST percentage (10%) quantiles. Please refer to Section 2.3.3 of the experiment design.

### 2.3.5. Statistical methodology

LST is a measurement of the temperature equivalent perceived by vegetation, and is commonly used in plant physiological studies (Sandholt et al., 2002). Increases in LST reflect the decreased partitioning of radiation to latent heat flux compared to sensible heat flux (Li et al., 2013; Shen et al., 2018). Thus, LST was used as an integrator of crop water and heat stress, and as the major limiting factor of cropland photosynthesis activity in this study.

We firstly averaged the values of testing pixels in LUE, SIF, EVI, and LST in each of the spatial-temporal LST groups. Time-series analysis was then applied to identify the seasonality of the averaged measurements from a ten-year span of monthly mean. Thereafter, we adopted the one-way analysis of variance (ANOVA) method (Welch, 1951) to determine whether there were any statistically significant differences among the means of the values in LUE and its related measurements with different spatial-temporal LST ranges. If the one-way ANOVA test yielded a significant result, Tukey's honestly significant difference (HSD) *post hoc* test (Tukey, 1949) was applied to examine all pairwise comparisons between the means of the measurements across every spatial-temporal LST level, identifying all differences between any two means of the measurements that were larger than the expected standard error.

In this study, data processing and statistical analysis were performed in the R computation environment (<http://cran.r-project.org>) (RCoreTeam, 2013). Partial visualization were generated using the Microsoft Excel package.

## 3. Results and discussion

### 3.1. The justification of datasets in multiple resolution and the calibration of the linear relationship of SIF to GPP

The results of the linear regressions between daytime flux tower-measured GPP with MODIS EVI at  $0.05^\circ$ ,  $0.1^\circ$  and  $0.5^\circ$  spatial resolutions (Fig. 2a–c respectively) reveal that there were slight differences among their regression coefficients. The finer the spatial resolution in EVI, the smaller the slope coefficient, and the larger the  $R^2$  value. When the EVI resolution was changed from  $0.05^\circ$  to  $0.5^\circ$  (i.e., 100 times coarser), the  $R^2$  dropped from 0.86 to 0.80, and the slope value increased by 4.7%. However, all regressions are statistically significant ( $p < 0.01$ ). The variances in flux GPP or EVI at  $0.5^\circ$  resolution can linearly explain 80% of each other. Thus, the direct comparison of flux GPP with the much coarser resolution of remotely sensed retrievals at  $0.5^\circ$  spatial resolution produced acceptable regressions at the eddy flux sites. In addition, Australian rainfed croplands are mostly characterized by broadacre planting (Hochman et al., 2017, 2012). Therefore, we assumed that the landscape in our study area is generally homogenous within several square kilometers.

Meanwhile, we compared the fit of linear regressions between

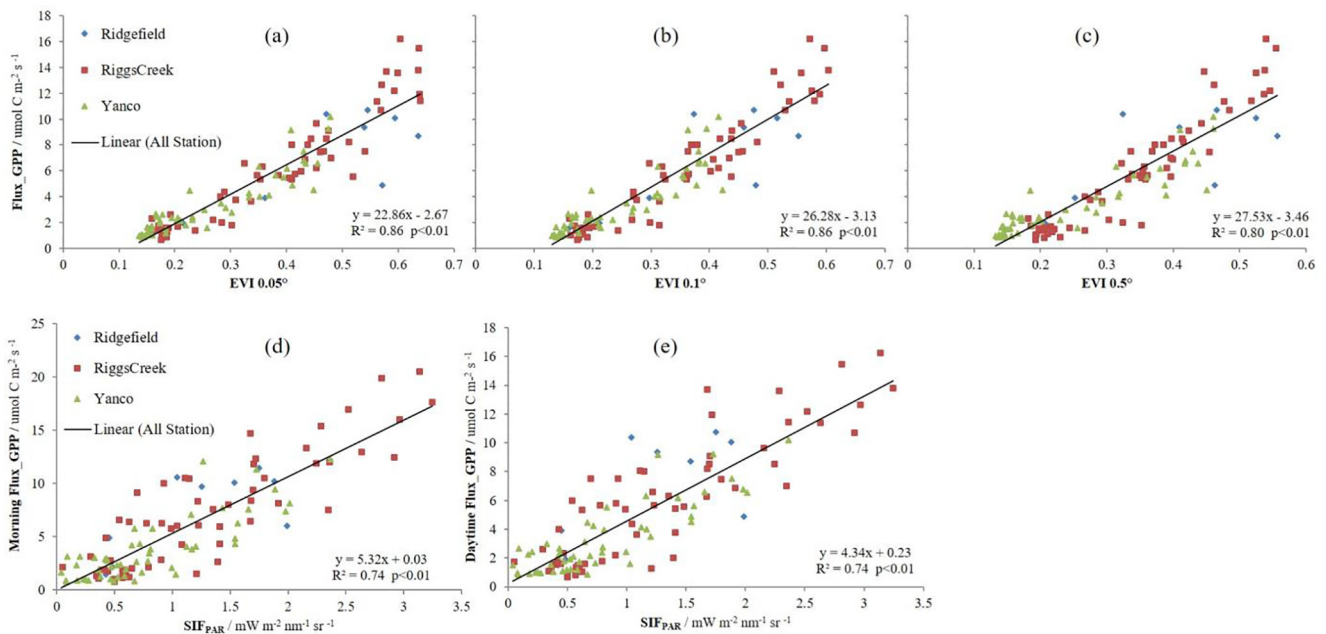


**Fig. 2.** Flux tower footprint calibrations. Morning Flux\_GPP is the monthly GPP averaged from half-hourly GPP data from 9:00 to 11:00 am. Daytime Flux\_GPP is averaged during the daytime. SIF<sub>PAR</sub> is PAR-normalized SIF.

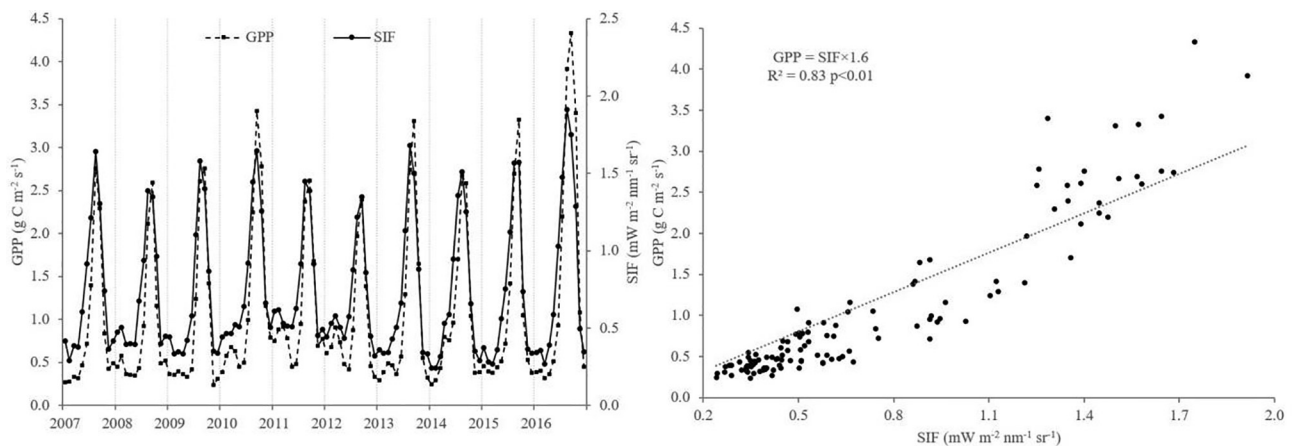


**Fig. 3.** The seasonal dynamics (left), and the relationship between monthly remote sensing-based gross primary production (GPP) and solar-induced chlorophyll fluorescence (SIF) (right), across the Australian rainfed cropland during 2007–2016.

satellite SIF<sub>PAR</sub> and morning average (09:00–11:00 am) flux GPP and daytime average flux GPP (Fig. 2d, e respectively). The determination coefficients, R<sup>2</sup>, were the same (0.74) and statistically significant (p < 0.01) for both regressions. These results indicate that the GOME-2 SIF observations, with an overpass time of around 9:30 am local time, linearly correlate with cropland GPP.

Admittedly, the existence of a linear relationship between GPP and SIF is a debatable issue in current research. The APAR can be theoretically divided into three distinct fractions: the energy required to fix carbon, to generate fluorescence, and to dissipate nonradiative heat (Verma et al., 2017). These three pathways may compete with each other (Meroni et al., 2009), especially at the instantaneous scale and leaf level. However, many recent empirical studies indicate that the linear relation of SIF to GPP is more robust at coarse spatial and temporal resolutions (such as ecosystem and regional scales) (Smith et al., 2018; Zhang et al., 2016; Lu et al., 2018; Miao et al., 2018; Zhang et al., 2018) than is suggested by theory based at leaf-level processes (Verma et al., 2017). At the same time, SIF captures the dynamics of seasonal and inter-annual GPP better than other remote sensing observations, especially for dryland ecosystems (Smith et al., 2018). Whereas, Li et al.

(2018) have revealed a nearly universal GPP-SIF relationship encompassing a variety of biomes globally. In this study, we provided additional empirical evidence in the Australian context (Fig. 2d, e) contributing to the public debate on GPP-SIF relationship. Fig. 3 shows the calibration of the value of a, the constant ratio of GPP to SIF, by incorporating the remote sensing-based OzWALD-GPP dataset for the 111 Australian rainfed cropland pixels. The independent SIF signal has shown high consistency with the GPP estimation in terms of seasonal dynamics during 2007–2016 (Fig. 3-left). Thus, a can be calculated from the empirical linear model between GPP estimation and SIF as 1.6 (p < 0.01) (Fig. 3-right). Further testing of other SIF and GPP datasets with finer spatial-temporal resolutions will be expected to improve the accuracy of this calibration.

### 3.2. Spatial pattern of LUE and its related measurements based on geographical latitude range

The seasonality in monthly canopy greenness (EVI) (Fig. 4c, d) indicate that there was one major crop growing season, from June to November, across both of the Australian rainfed cropland belts. The

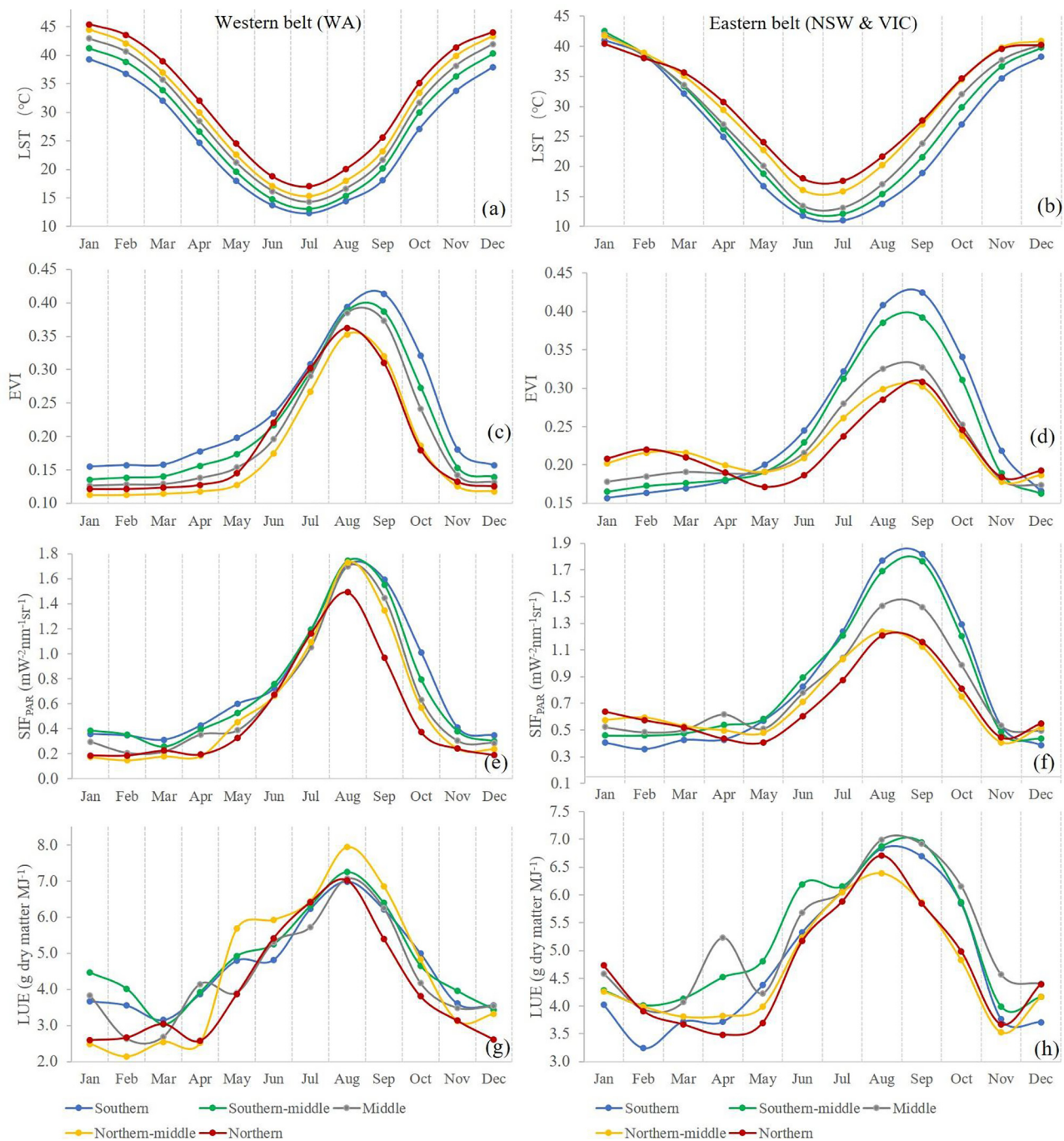


**Fig. 4.** Spatial patterns in ten-year mean seasonality of LST, EVI,  $SIF_{PAR}$  and LUE. The two columns of panels are for the western (left) and eastern (right) belts of Australian rainfed croplands. The rows of panels present LST (a, b), EVI (c, d),  $SIF_{PAR}$  (e, f), and LUE (g, h).  $SIF_{PAR}$  is PAR-normalized SIF.

start and end months of each growing season were consistent among the five LST zones, which are May and November in the western belt (Fig. 4c) and June and November in the eastern belt (Fig. 4d). These findings suggest that the months of sowing and harvesting winter crops were consistent from south to north across the Australian broadacre rainfed cropland. The EVI values peaked in September across all zones in the eastern belt (NSW and VIC) and the Southern zone in the western belt (WA). Peaks in EVI were observed in August across all other zones in the western belt.

As shown in Fig. 4a and b, the LST curves exhibited a spatial gradient across both of the cropland belts (Fig. 4a, b). The average LST level gradually reduced from north to south. Correspondingly, the cooler the region, the higher the amplitude of EVI curves (Fig. 4c, d).

These results were typical in the eastern belt, as well as in the middle, southern-middle, and southern zones in the western belt. This negative relationship between LST and EVI indicates that the winter crops grow better and the cropland canopy is greener in the relatively cooler (southern) regions of Australian croplands. This also indicates that the growth of Australian winter crops is sensitive to the increase of LST.

In addition, the results show that there was also one major cycle of increase, peak and decrease in the rates of photosynthesis signal  $SIF_{PAR}$  (Fig. 4e, f). The seasonality of PAR-normalized SIF was constant with EVI in terms of start and end months; however, the peak month for SIF was August in the northern and northern-middle zones of the eastern cropland belt, as well as in all zones of the western belt. Geographically, the amplitude of the SIF seasonality curve was highest in the cooler

**Table 2**  
Statistical summary of satellite-based LST, EVI, SIF and LUE across all sites during the growing season.

	LST (°C)		SIF <sub>PAR</sub> (mW <sup>-2</sup> nm <sup>-1</sup> sr <sup>-1</sup> )		EVI		LUE (g dry matter MJ <sup>-1</sup> )	
	Mean	SE	Mean	SE	Mean	SE	Mean	SE
June	14.4	0.08	0.74	0.01	0.22	0.002	5.23	0.05
July	13.5	0.08	1.11	0.02	0.29	0.002	5.95	0.05
Aug	16.5	0.10	1.54	0.02	0.37	0.003	6.70	0.04
Sep	21.9	0.14	1.45	0.02	0.37	0.003	6.22	0.04
Oct	30.5	0.15	0.92	0.02	0.28	0.003	5.04	0.04
Nov	36.9	0.14	0.43	0.01	0.18	0.002	3.70	0.04

\*SE is one standard error.

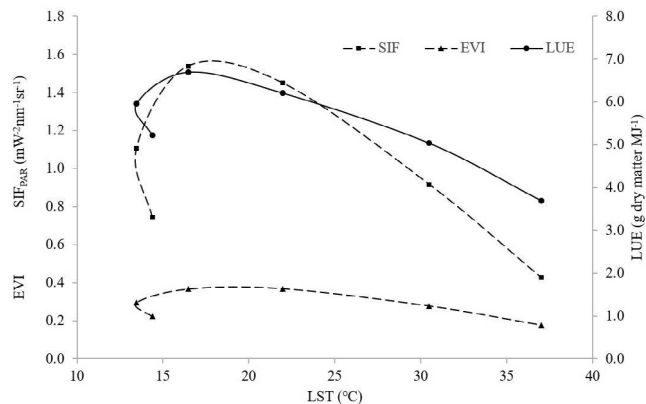


**Fig. 5.** Seasonal dynamics of average monthly LST, SIF, EVI, and LUE across Australian rainfed cropland belts.

southern zone and lowest in the warmer northern zone in both cropland belts. These results indicate a constant spatial pattern of the satellite-based observations in EVI and SIF.

By contrast, there was more inter-monthly variation in LUE than in EVI or SIF (Fig. 4). Satellite-based LUE ranged between 3.4 and 7.0 and 2.1–7.8 g dry matter MJ<sup>-1</sup> in the eastern and western belts respectively (Fig. 4g, h). August was generally the peak month for LUE across the entire study area, with the exception that the cooler southern LST zone of the eastern belt displayed peaks during September. During the growing season, average LUE values in the middle LST zone were greatest in the eastern belt, while largest in the northern-middle LST zone in the western belt. This indicates a spatial non-linear relationship between LUE and LST. In terms of seasonality, the rate of decline in LUE after August was greater than the rate of LUE increases before August, implying a seasonal asymmetry in LUE in response to surface temperature change across Australian rainfed croplands throughout the

**Table 3**  
Pairwise comparison among the growing season months for LUE and its related measurements.

p value	June	July	Aug	Sep	Oct	June	July	Aug	Sep	Oct
	LST (°C)					SIF <sub>PAR</sub> (mW <sup>-2</sup> nm <sup>-1</sup> sr <sup>-1</sup> )				
July	< 0.01					< 0.01				
Aug	< 0.01	< 0.01				< 0.01	< 0.01			
Sep	< 0.01	< 0.01	< 0.01			< 0.01	< 0.01	< 0.01		
Oct	< 0.01	< 0.01	< 0.01	< 0.01		< 0.01	< 0.01	< 0.01	< 0.01	
Nov	< 0.01	< 0.01	< 0.01	< 0.01	< 0.01	< 0.01	< 0.01	< 0.01	< 0.01	< 0.01
	EVI					LUE (g dry matter MJ <sup>-1</sup> )				
July	< 0.01					< 0.01				
Aug	< 0.01	< 0.01				< 0.01	< 0.01			
Sep	< 0.01	< 0.01	1.00			< 0.01	0.09	< 0.01		
Oct	< 0.01	< 0.01	< 0.01	< 0.01		0.83	< 0.01	< 0.01	< 0.01	
Nov	< 0.01	< 0.01	< 0.01	< 0.01	< 0.01	< 0.01	< 0.01	< 0.01	< 0.01	< 0.01

winter crop's life span.

### 3.3. Inter-seasonal dynamics of LUE and its related measurements

The cropland vegetation greenness change and the photosynthetic active seasonality are theoretically determined by the meteorological cycle. Each of the months throughout the growing season has a certain level of LST; the EVI, SIF and LUE values are thus expected to be at corresponding levels. Table 2 and Fig. 5 present the ten-year average status for each of the satellite-based vegetation measurements from June to November (the average growing season).

Across all years (2007–2016), the largest EVI value occurred in September, while SIF and LUE reached their largest values in August. July was the coldest month across all sites, with the lowest LST; however, this did not coincide with the smallest greenness index (EVI) or the least photosynthetic activity (SIF and LUE). The smallest EVI, SIF and LUE occurred in November, the hottest month during the major growing season across Australian rainfed croplands. This indicates that Australian rainfed crops tend to exhibit a higher rate of photosynthesis activity in a lower LST range, especially in the crop reproductive growth stage (the stage after the peak EVI month during growing season).

Through pairwise comparisons of each of the mean satellite-based measurements among the growing season months (Table 3), we observed that average EVIs during August and September were not statistically different ( $p > 0.1$ ) across the areas studied. By contrast, SIF values varied significantly throughout the months of the growing season ( $p < 0.05$ ). This implies that the cropland photosynthetic activity is variable despite the vegetation greenness remaining constant. We also observed that LUE showed a distinct value in August compared to other months of the growing season ( $p < 0.01$ ). In this case, LUE values in June and in October did not differ significantly ( $p > 0.1$ ). The difference in mean LUE values between July and September was of marginal significance ( $0.1 > p > 0.05$ ). Thus, the inter-seasonal dynamics of LUE are non-symmetrical across Australian rainfed croplands. Fig. 5 also presents the hysteresis nature of the observations in LUE, EVI and SIF response to LST.

### 3.4. Intra-seasonal dynamics of LUE based on LST percentage quantiles

Fig. 6a visualizes the LST ranges and means for each spatial-temporal percentage (10%) quantile for LST within each month of the growing season. The range of LST in each month overlapped with the ranges in the months before and after. All levels of mean LST within each month were significantly different from each other (all pairwise  $p < 0.05$ ). The standard deviations (Sd) in the first and last 10% quantiles for LST, were greater than those of other percentage quantiles in each month from June to November (Fig. 6a). These results indicate that every month during the growing season featured pixels with

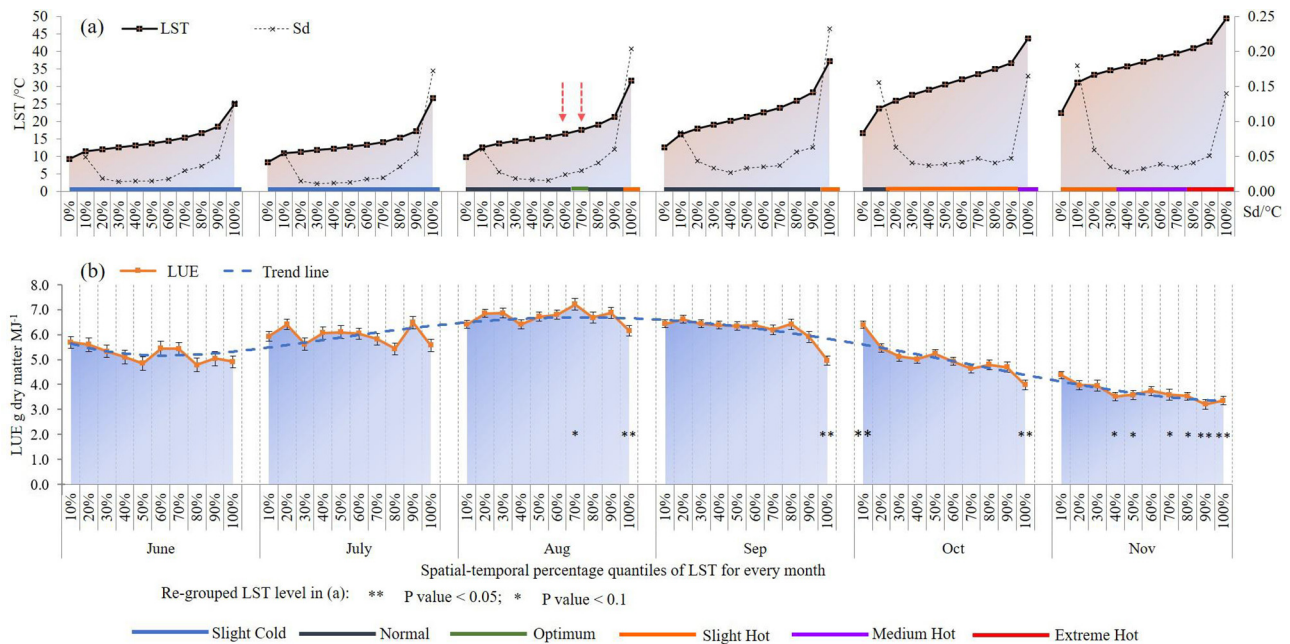


**Fig. 6.** Re-grouped spatial-temporal LST levels from June to November by one-way ANOVA and *post hoc* test. (a) Spatial-temporal percentage quantile LST levels for each month from June to November. (b) One-way ANOVA and *post hoc* test of the mean LUE for corresponding spatial-temporal percentage quantile LST levels. All pairwise comparison tests of mean temperature among LST levels in each month have a statistically significant p value of < 0.05.

extremely high values in LST.

By comparing the mean values for LUE across different groups of LST data using one-way ANOVA and *post-hoc* testing, we then re-grouped the spatial-temporal LST into six ranges, as shown in the horizontal colored bars in Fig. 6a. Thereafter, we attributed each of the six statistical LST ranges to the following groups based on their LST means: slight cold, normal, optimum, slight hot, medium hot, and extreme hot (Fig. 6a). Mean LUE significantly ( $p < 0.1$ ) peaked at the optimum LST range of 16.6–17.6 °C in the seventh 10% quantile of LST in August (Fig. 6b). An LST value lower or higher than this range in August resulted in lower LUE values. Admittedly, each of the key phenological stages of the crops has its optimal LST range for crop growth. The site-based study of Porter and Gawith (1999) demonstrated that the optimum air temperatures for winter wheat are 10.6 °C (terminal spikelet), 21.0 °C (anthesis), and 20.7 °C (grain-filling). Wardlaw and Moncur (1995) also concluded that the optimum air temperature range for wheat during the vegetative stage is 9–16 °C. These results are constant with our satellite-based findings. As shown in Fig. 6a, there was no significant LUE increase or decrease in any of the 10% quantiles of LST groups during the vegetative growth stage (primarily in June and July). This suggests that the LST range in 8.4–16.6 °C (the first 10% quantile of LST in June—the sixth 10% quantile of LST in August) is suitable for the vegetative growth of Australian winter wheat. Moreover, during the reproductive growth stage (primarily in September to November), the pixels with LST values that were in the first 10% quantile of LST group during October had the highest LUE values; the LST level was 21.6 °C. Australian winter wheat growth in October observed from space, was found to roughly correspond to the site-based crop grain-filling stage. The site-based results from Wardlaw and Moncur (1995) and Porter and Gawith (1999) have further supported our findings. This consistency has revealed the potential to remotely monitor large-scale LUE by introducing the measurements of SIF and EVI.

It is noteworthy that the mean LUE values were significantly reduced ( $p < 0.05$ ) when LST was in the highest 10% quantile during all months of the reproductive stage (Fig. 6b). Every month has its particular water and heat patterns, corresponding to the particular stages of crop growth over a specific crop’s life span. During each of the months

in the reproductive growth stage, the pixels in the uppermost 10% quantile in LST exhibit extreme higher LST level than the particular average water and heat pattern. These lead to stresses on photosynthetic efficiency throughout all the months in the reproductive stage.

The non-linear relationship between LUE and LST was also observed in the re-grouped temporal-spatial LST categories (Fig. 6b). During June and July (the vegetative growth stage), all 10% quantile of LST were categorized into one group with the lowest average LST value. By contrast, there were significant LUE decreases in the uppermost 10% quantile of the LST groups in October, as well as in six of the 10% LST quantiles in November (late reproductive growth stage) (Fig. 6b). These observations indicate that LUE increased more slowly (was less sensitive) as LST increased from the minimum to the optimum range (16.6–17.6 °C during August), then declined more rapidly (was more sensitive) as LST increased from the optimal to the higher LST ranges, particularly during October and November. These results imply the non-symmetrical relationship of LUE response to LST. The suitable LST ranges for cropland photosynthesis activities vary at different crop growth stages. Thus, assigning a single threshold for LST in the 20–30 °C range, as has been applied in the formulations of some current remote sensing-based GPP models, could result in bias if inter- and intra-seasonal variations in optimum LST are not considered.

The optimum LST range occurred in August, which is also one of the peak EVI month in Australian rainfed cropland (Fig. 5). Whereas, there were three spatial-temporal LST categories (i.e. normal, optimum, and slight hot) were identified in August. We therefore examined the spatial-temporal distributions of pixels in each of the three LST categories.

Pixels in the three LST ranges were distributed in different geographical regions across Australian rainfed croplands (Fig. 7). Most of the pixels in the optimum LST category with the highest LUE level in August were gathered in the geographical south-middle zones across both of the eastern and western belts. Pixels in the slightly hot LST range were distributed in the upper northern part of the eastern belt, as well as the western belt in some hydrologically dry years (2007, 2009, 2012, 2013 and 2014) (Cleverly et al., 2016; Dijk et al., 2013). Meanwhile, the pixels in the normal LST range were distributed in a scatter formation from the northern-middle zone to the southern zones across

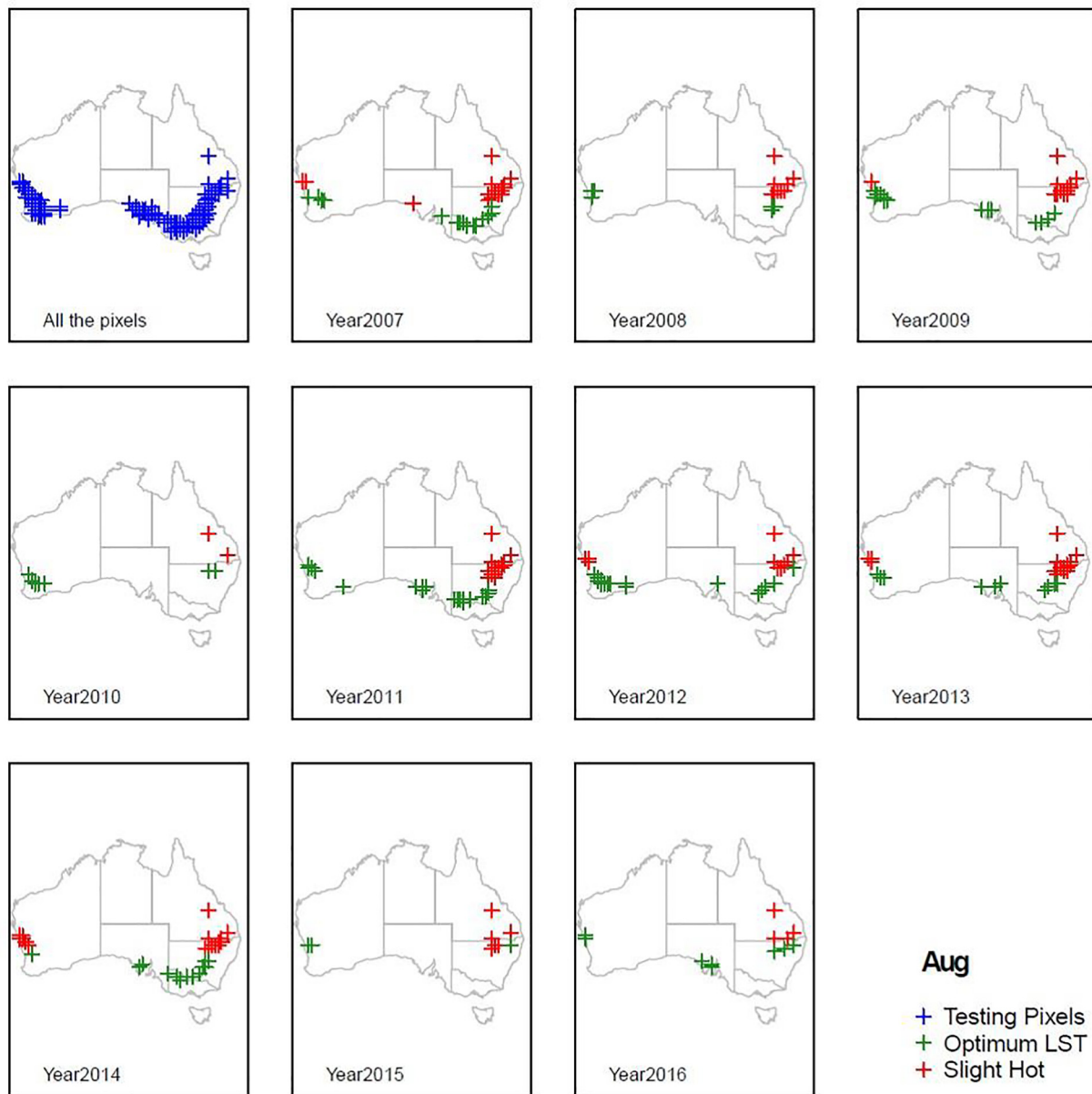


Fig. 7. Spatial-temporal distributions of pixels within the re-grouped LST levels during August across all ten years.

the whole study area. Temporally, the year 2011 showed the most pixels (19) with the optimum LST range in August, while the years 2008 and 2015 had the smallest number of pixels with the optimal LST range (6 and 3 pixels respectively). According to the Australian Bureau of Meteorology (<http://www.bom.gov.au/climate/change/>), year 2011 was recorded as has the most sufficient rainfall (707.7 mm/yr) in Australia during 2007–2016. While year 2008 and 2015 have the least amount of annual rainfall (446.3 and 478.7 mm/yr) as recorded. These indicated that, the amount of annual rainfall is one of the key environmental limiting factors to crop LUE across Australian rainfed croplands.

#### 4. Conclusions

We examined the spatial pattern and the inter- and intra-seasonal dynamics of Australian rainfed cropland photosynthesis activity entirely by means of satellite-based measurements. LUE was calculated as the ratio of  $SIF_{PAR}$  to EVI, followed by multiplication by a constant coefficient. The coefficient was calibrated by a set of remote sensing-

based estimates in this study. The measurements of SIF and EVI provide direct estimate of vegetation photosynthetic activity and greenness, respectively. The link between SIF and crop photosynthesis was found to be instantaneous, but the satellite SIF signal often contains additional information pertaining to canopy structure and total canopy chlorophyll content (Yang et al., 2017). The advance arised in our methodology is to effectively remove the relative constant greenness level (EVI as fPAR) so as to estimate the spatial-temporal photosynthetic activity entirely from remotely sensed variables.

This study further demonstrated the spatial pattern and seasonal dynamics of LUE and its related measurements both throughout the cropland growing season and within each month over a range of temporal-spatial LST percentage quantiles. Spatially, the gradients in the seasonality of EVI and SIF were observed opposite to the LST gradients from the northern to southern regions of the two cropland belts in Australia. In contrast, the amplitude of the LUE curves were largest in the middle zone in the eastern belt and southern-middle zone in the western belt, instead of in the northern (warmest) or southern (coolest) zones (Fig. 4). Intra-seasonally, LUE peaked at the seventh 10%

quantile of LST range of 16.6–17.6 °C in August (Fig. 6). The present results also reveal the nonsymmetric responses of LUE to surface temperatures spatially, seasonally and during certain months.

Overall, our study approximated LUE entirely through remotely sensed variables. By using LST, a proxy of the integrated environmental stress, we related the cropland photosynthesis activity to the spatial and seasonal variation in optimum LST, the findings are important for crop management and crop yield modeling in rainfed cropping systems. As such, this study has implications for the large-scale detection and monitoring of cropland water and heat stress under a future warmer and drier climate.

## Acknowledgments

The authors wish to thank Dr. Mingming Cheng and Dr. Hao Shi for their helpful suggestions for this study. We are grateful to the anonymous reviewers and the editors for their insightful comments in improving the quality of this paper. The data support from Geoscience Australia (<http://www.ga.gov.au/>) and Australian Water and Landscape Dynamics group (<http://www.wenfo.org/wald/>) is also gratefully acknowledged.

## References

- Beringer, J., McHugh, I., Hutley, L.B., Isaac, P., Kljun, N., 2017. Technical note: dynamic Integrated Gap-filling and partitioning for OzFlux (DINGO). *Biogeosciences* 14, 1457–1460.
- Berry, J., Bjorkman, O., 1980. Photosynthetic response and adaptation to temperature in higher plants. *Annu. Rev. Plant Physiol.* 31, 491–543.
- Bowden, P., Edwards, J., Ferguson, N., Nee, T.M., Manning, B., Roberts, K., Schipp, A., Schulze, K., Wilkins, J., 2008. *Wheat Growth and Development*. NSW Department of Primary Industries.
- Broich, M., Huete, A., Paget, M., Ma, X., Tulbure, M., Coupe, N.R., Evans, B., Beringer, J., Devadas, R., Davies, K., Held, A., 2015. A spatially explicit land surface phenology data product for science, monitoring and natural resources management applications. *Environ. Modell. Software* 64, 191–204.
- Campbell, P.K.E., Middleton, E.M., Corp, L.A., Kim, M.S., 2008. Contribution of chlorophyll fluorescence to the apparent vegetation reflectance. *Sci. Total Environ.* 404, 433–439.
- Cleverly, J., Eamus, D., Luo, Q., Restrepo Coupe, N., Kljun, N., Ma, X., Ewenz, C., Li, L., Yu, Q., Huete, A., 2016. The importance of interacting climate modes on Australia's contribution to global carbon cycle extremes. *Sci. Rep.* 6, 23113.
- Dan, L., Ji, J., He, Y., 2007. Use of ISLSCP II data to intercompare and validate the terrestrial net primary production in a land surface model coupled to a general circulation model. *J. Geophys. Res. Atmos.* 112.
- Dijk, A.I., Beck, H.E., Crosbie, R.S., Jeu, R.A., Liu, Y.Y., Podger, G.M., Timbal, B., Viney, N.R., 2013. The millennium drought in southeast Australia (2001–2009): natural and human causes and implications for water resources, ecosystems, economy, and society. *Water Resour. Res.* 49, 1040–1057.
- Dong, J., Xiao, X., Wagler, P., Zhang, G., Zhou, Y., Jin, C., Torn, M.S., Meyers, T.P., Suyker, A.E., Wang, J., Yan, H., Biradar, C., Moore, B., 2015. Comparison of four EVI-based models for estimating gross primary production of maize and soybean croplands and tallgrass prairie under severe drought. *Remote Sens. Environ.* 162, 154–168.
- Gamon, J., Qiu, H., 1999. Ecological applications of remote sensing at multiple scales. In: *Handbook of Functional Plant Ecology* 805. pp. 846.
- Garbulsky, M.F., Peñuelas, J., Papale, D., Filella, I., 2008. Remote estimation of carbon dioxide uptake by a Mediterranean forest. *Glob. Change Biol.* 14, 2860–2867.
- Gitelson, A.A., Gamon, J.A., 2015. The need for a common basis for defining light-use efficiency: Implications for productivity estimation. *Remote Sens. Environ.* 156, 196–201.
- Gitelson, A.A., Merzlyak, M.N., 1996. Signature analysis of leaf reflectance spectra: algorithm development for remote sensing of chlorophyll. *J. Plant Physiol.* 148, 494–500.
- Gitelson, A.A., Peng, Y., Arkebauer, T.J., Suyker, A.E., 2015. Productivity, absorbed photosynthetically active radiation, and light use efficiency in crops: implications for remote sensing of crop primary production. *J. Plant Physiol.* 177, 100–109.
- Guan, K., Berry, J.A., Zhang, Y., Joiner, J., Guanter, L., Badgley, G., Lobell, D.B., 2016. Improving the monitoring of crop productivity using spaceborne solar-induced fluorescence. *Glob. Change Biol.* 22, 716–726.
- Guanter, L., Zhang, Y., Jung, M., Joiner, J., Voigt, M., Berry, J.A., Frankenberg, C., Huete, A.R., Zarco-Tejada, P., Lee, J.-E., Moran, M.S., Ponce-Campos, G., Beer, C., Camps-Valls, G., Buchmann, N., Gianelle, D., Klumpp, K., Cescatti, A., Baker, J.M., Griffis, T.J., 2014. Global and time-resolved monitoring of crop photosynthesis with chlorophyll fluorescence. *Proc. Natl. Acad. Sci. U.S.A.* 111, E1327–E1333.
- Hilker, T., Coops, N.C., Wulder, M.A., Black, T.A., Guy, R.D., 2008. The use of remote sensing in light use efficiency based models of gross primary production: a review of current status and future requirements. *Sci. Total Environ.* 404, 411–423.
- Hochman, Z., Gobbett, D., Holzworth, D., McClelland, T., van Rees, H., Marinoni, O., Garcia, J.N., Horan, H., 2012. Quantifying yield gaps in rainfed cropping systems: a case study of wheat in Australia. *Field Crops Res.* 136, 85–96.
- Hochman, Z., Gobbett, D.L., Horan, H., 2017. Climate trends account for stalled wheat yields in Australia since 1990. *Glob. Change Biol.* 23, 2071–2081.
- Huete, A., Didan, K., Miura, T., Rodriguez, E.P., Gao, X., Ferreira, L.G., 2002. Overview of the radiometric and biophysical performance of the MODIS vegetation indices. *Remote Sens. Environ.* 83, 195–213.
- Huete, A.R., 2012. Vegetation indices, remote sensing and forest monitoring. *Geogr. Compass* 6, 513–532.
- Idso, S.B., Jackson, R.D., Reginato, R.J., 1977. Remote sensing for agricultural water management and crop yield prediction. *Agric. Water Manage.* 1, 299–310.
- Jeong, S.-J., Schimel, D., Frankenberg, C., Drewry, D.T., Fisher, J.B., Verma, M., Berry, J.A., Lee, J.-E., Joiner, J., 2017. Application of satellite solar-induced chlorophyll fluorescence to understanding large-scale variations in vegetation phenology and function over northern high latitude forests. *Remote Sens. Environ.* 190, 178–187.
- Joiner, J., Guanter, L., Lindstrot, R., Voigt, M., Vasilkov, A., Middleton, E., Huemmrich, K., Yoshida, Y., Frankenberg, C., 2013. Global monitoring of terrestrial chlorophyll fluorescence from moderate spectral resolution near-infrared satellite measurements: methodology, simulations, and application to GOME-2. *Atmos. Meas. Tech.* 6, 2803–2823.
- Joiner, J., Yoshida, Y., Vasilkov, A.P., Corp, L.A., Middleton, E.M., 2011. First observations of global and seasonal terrestrial chlorophyll fluorescence from space. *Biogeosciences* 8, 637–651.
- Joiner, J., Yoshida, Y., Vasilkov, A.P., Schaefer, K., Jung, M., Guanter, L., Zhang, Y., Garrity, S., Middleton, E.M., Huemmrich, K.F., Gu, L., Belleli Marchesini, L., 2014. The seasonal cycle of satellite chlorophyll fluorescence observations and its relationship to vegetation phenology and ecosystem atmosphere carbon exchange. *Remote Sens. Environ.* 152, 375–391.
- Li, X., Xiao, J., He, B., Altaf Arain, M., Beringer, J., Desai, A.R., Emmel, C., Hollinger, D.Y., Krasnova, A., Mammarella, I., 2018. Solar-induced chlorophyll fluorescence is strongly correlated with terrestrial photosynthesis for a wide variety of biomes: first global analysis based on OCO-2 and flux tower observations. *Glob. Change Biol.* 24, 3990–4008.
- Li, Z.-L., Tang, B.-H., Wu, H., Ren, H., Yan, G., Wan, Z., Trigo, I.F., Sobrino, J.A., 2013. Satellite-derived land surface temperature: current status and perspectives. *Remote Sens. Environ.* 131, 14–37.
- Liu, L., Cheng, Z., 2010. Detection of vegetation light-use efficiency based on solar-induced chlorophyll fluorescence separated from canopy radiance spectrum. *IEEE J. Sel. Top. Appl. Earth Obs. Remote Sens.* 3, 306–312.
- Liu, L., Zhang, Y., Jiao, Q., Peng, D., 2013. Assessing photosynthetic light-use efficiency using a solar-induced chlorophyll fluorescence and photochemical reflectance index. *Int. J. Remote Sens.* 34, 4264–4280.
- Lobell, D.B., Hicke, J.A., Asner, G.P., Field, C.B., Tucker, C.J., Los, S.O., 2002. Satellite estimates of productivity and light use efficiency in United States agriculture, 1982–98. *Glob. Change Biol.* 8, 722–735.
- Lu, X., Cheng, X., Li, X., Chen, J., Sun, M., Ji, M., He, H., Wang, S., Li, S., Tang, J., 2018. Seasonal patterns of canopy photosynthesis captured by remotely sensed sun-induced fluorescence and vegetation indexes in mid-to-high latitude forests: a cross-platform comparison. *Sci. Total Environ.* 644, 439–451.
- Lymburner, L., Tan, P., Mueller, N., Thackway, R., Lewis, A., Thankappan, M., Randall, L., Islam, A., Senarath, U., 2010. 250 metre Dynamic Land Cover Dataset of Australia. Geoscience Australia, Canberra.
- Meroni, M., Rossini, M., Guanter, L., Alonso, L., Rascher, U., Colombo, R., Moreno, J., 2009. Remote sensing of solar-induced chlorophyll fluorescence: review of methods and applications. *Remote Sens. Environ.* 113, 2037–2051.
- Miao, G., Guan, K., Yang, X., Bernacchi, C.J., Berry, J.A., Delucia, E.H., Wu, J., Moore, C.E., Meacham, K., Cai, Y., Peng, B., Kimm, H., Masters, M.D., 2018. Sun-induced chlorophyll fluorescence, photosynthesis, and light use efficiency of a soybean field from seasonally continuous measurements. *J. Geophys. Res. Biogeosci.* 123, 610–623.
- Monteith, J.L., 1972. Solar radiation and productivity in tropical ecosystems. *J. Appl. Ecol.* 9, 747–766.
- Monteith, J.L., 1977. Climate and the efficiency of crop production in Britain [and discussion]. *Philos. Trans. R. Soc. Lond. B: Biol. Sci.* 281, 277–294.
- Porter, J.R., Gawith, M., 1999. Temperatures and the growth and development of wheat: a review. *Eur. J. Agron.* 10, 23–36.
- RCORETEAM, 2013. R: A Language and Environment for Statistical Computing. [WWW document]. R Foundation for Statistical Computing, Vienna, Austria. <http://www.R-project.org>.
- Running, S.W., Nemani, R., Glassy, J.M., Thornton, P.E., 1999. MODIS Daily Photosynthesis (PSN) and Annual Net Primary Production (NPP) Product (MOD17) Algorithm Theoretical Basis Document. University of Montana SCF At-Launch Algorithm ATBD Documents (available online at: [www.nsg.umt.edu/modis/ATBD/ATBD\\_MOD17\\_v21.Pdf](http://www.nsg.umt.edu/modis/ATBD/ATBD_MOD17_v21.Pdf)).
- Running, S.W., Nemani, R.R., Heinsch, F.A., Zhao, M., Reeves, M., Hashimoto, H., 2004. A continuous satellite-derived measure of global terrestrial primary production. *Bioscience* 54, 547–560.
- Sandholt, I., Rasmussen, K., Andersen, J., 2002. A simple interpretation of the surface temperature/vegetation index space for assessment of surface moisture status. *Remote Sens. Environ.* 79, 213–224.
- Shen, J., Huete, A., Tran, N.N., Devadas, R., Ma, X., Eamus, D., Yu, Q., 2018. Diverse sensitivity of winter crops over the growing season to climate and land surface temperature across the rainfed cropland-belt of eastern Australia. *Agric. Ecosyst. Environ.* 254, 99–110.
- Sims, D.A., Rahman, A.F., Cordova, V.D., El-Masri, B.Z., Baldocchi, D.D., Bolstad, P.V., Flanagan, L.B., Goldstein, A.H., Hollinger, D.Y., Misson, L., Monson, R.K., Oechel, W.C., Schmid, H.P., Wofsy, S.C., Xu, L., 2008. A new model of gross primary

- productivity for North American ecosystems based solely on the enhanced vegetation index and land surface temperature from MODIS. *Remote Sens. Environ.* 112, 1633–1646.
- Sjöström, M., Ardö, J., Arneht, A., Boulain, N., Cappelaere, B., Eklundh, L., de Grandcourt, A., Kutsch, W.L., Merbold, L., Nouvellon, Y., Scholes, R.J., Schubert, P., Seaquist, J., Veenendaal, E.M., 2011. Exploring the potential of MODIS EVI for modeling gross primary production across African ecosystems. *Remote Sens. Environ.* 115, 1081–1089.
- Smith, W.K., Biederman, J.A., Scott, R.L., Moore, D.J.P., He, M., Kimball, J.S., Yan, D., Hudson, A., Barnes, M.L., Macbean, N., Fox, A.M., Litvak, M.E., 2018. Chlorophyll fluorescence better captures seasonal and interannual gross primary productivity dynamics across dryland ecosystems of southwestern North America. *Geophys. Res. Lett.* 45, 748–757.
- Tukey, J.W., 1949. Comparing individual means in the analysis of variance. *Biometrics* 99–114.
- Verma, M., Schimel, D., Evans, B., Frankenberg, C., Beringer, J., Drewry, D.T., Magney, T., Marang, I., Hutley, L., Moore, C., Eldering, A., 2017. Effect of environmental conditions on the relationship between solar-induced fluorescence and gross primary productivity at an OzFlux grassland site. *J. Geophys. Res. Biogeosci.* 122, 716–733.
- Wang, Z., Xiao, X., Yan, X., 2010. Modeling gross primary production of maize cropland and degraded grassland in northeastern China. *Agric. For. Meteorol.* 150, 1160–1167.
- Wardlaw, I., Moncur, L., 1995. The response of wheat to high temperature following anthesis. I. The rate and duration of kernel filling. *Funct. Plant Biol.* 22, 391–397.
- Welch, B., 1951. On the comparison of several mean values: an alternative approach. *Biometrika* 38, 330–336.
- Xiao, J., Zhuang, Q., Baldocchi, D.D., Law, B.E., Richardson, A.D., Chen, J., Oren, R., Starr, G., Noormets, A., Ma, S., Verma, S.B., Wharton, S., Wofsy, S.C., Bolstad, P.V., Burns, S.P., Cook, D.R., Curtis, P.S., Drake, B.G., Falk, M., Fischer, M.L., Foster, D.R., Gu, L., Hadley, J.L., Hollinger, D.Y., Katul, G.G., Litvak, M., Martin, T.A., Matamala, R., McNulty, S., Meyers, T.P., Monson, R.K., Munger, J.W., Oechel, W.C., Paw, U.K.T., Schmid, H.P., Scott, R.L., Sun, G., Suyker, A.E., Torn, M.S., 2008. Estimation of net ecosystem carbon exchange for the conterminous United States by combining MODIS and AmeriFlux data. *Agric. For. Meteorol.* 148, 1827–1847.
- Xiao, X., Hollinger, D., Aber, J., Goltz, M., Davidson, E.A., Zhang, Q., Moore, B., 2004. Satellite-based modeling of gross primary production in an evergreen needleleaf forest. *Remote Sens. Environ.* 89, 519–534.
- Xiao, X., Qingyuan, Z., Hollinger, D., Aber, J., Moore, B., 2005. Modeling gross primary production of an evergreen needleleaf forest using modis and climate data. *Ecol. Appl.* 15, 954–969.
- Yan, H., Fu, Y., Xiao, X., Huang, H.Q., He, H., Ediger, L., 2009. Modeling gross primary productivity for winter wheat–maize double cropping system using MODIS time series and CO<sub>2</sub> eddy flux tower data. *Agric. Ecosyst. Environ.* 129, 391–400.
- Yan, W., Zhong, Y., Shanguan, Z., 2017. Contrasting responses of leaf stomatal characteristics to climate change: a considerable challenge to predict carbon and water cycles. *Glob. Change Biol.* 716–726.
- Yang, H., Yang, X., Zhang, Y., Heskel, M.A., Lu, X., Munger, J.W., Sun, S., Tang, J., 2017. Chlorophyll fluorescence tracks seasonal variations of photosynthesis from leaf to canopy in a temperate forest. *Glob. Change Biol.* 23, 2874–2886.
- Yang, Y., Shang, S., Guan, H., Jiang, L., 2013. A novel algorithm to assess gross primary production for terrestrial ecosystems from MODIS imagery. *J. Geophys. Res. Biogeosci.* 118, 590–605.
- Yebra, M., van Dijk, A.I.J.M., Leuning, R., Guerschman, J.P., 2015. Global vegetation gross primary production estimation using satellite-derived light-use efficiency and canopy conductance. *Remote Sens. Environ.* 163, 206–216.
- Yu, Q., Hengsdijk, H., Liu, J.D., 2001. Application of a progressive-difference method to identify climatic factors causing variation in the rice yield in the Yangtze Delta, China. *Int. J. Biometeorol.* 45, 53–58.
- Yuan, W., Liu, S., Yu, G., Bonnefond, J.-M., Chen, J., Davis, K., Desai, A.R., Goldstein, A.H., Gianelle, D., Rossi, F., Suyker, A.E., Verma, S.B., 2010. Global estimates of evapotranspiration and gross primary production based on MODIS and global meteorology data. *Remote Sens. Environ.* 114, 1416–1431.
- Zhang, Y., Guanter, L., Berry, J.A., van der Tol, C., Yang, X., Tang, J., Zhang, F., 2016. Model-based analysis of the relationship between sun-induced chlorophyll fluorescence and gross primary production for remote sensing applications. *Remote Sens. Environ.* 187, 145–155.
- Zhang, Y., Xiao, X., Zhang, Y., Wolf, S., Zhou, S., Joiner, J., Guanter, L., Verma, M., Sun, Y., Yang, X., Paul-Limoges, E., Gough, C.M., Wohlfahrt, G., Gioli, B., van der Tol, C., Yann, N., Lund, M., de Grandcourt, A., 2018. On the relationship between sub-daily instantaneous and daily total gross primary production: implications for interpreting satellite-based SIF retrievals. *Remote Sens. Environ.* 205, 276–289.
- Zhao, M., Heinsch, F.A., Nemani, R.R., Running, S.W., 2005. Improvements of the MODIS terrestrial gross and net primary production global data set. *Remote Sens. Environ.* 95, 164–176.